HW-DFT-Based Measurement Method of Frequency-Coupling Characteristics Considering Fundamental Frequency Deviation for Stability Analysis

Meng Li, *Graduate Student Member, IEEE*, Heng Nian, *Senior Member, IEEE*, Han Li, Bin Hu, *Student Member, IEEE*, Yuming Liao, *Graduate Student Member, IEEE*, Haipan Li, Yiming Liu, and Yaoxin Wang

***Abstract*—Impedance measurement is an effective method to obtain the impedance characteristic of the renewable power generator. Discrete Fourier transformation (DFT) is commonly used to extract measurement signals. However, when there is a slight fundamental frequency deviation (FFD), the frequency resolution of DFT may be insufficient due to spectral leakage (SL). Under this circumstance, the measurement signals will be overlapped with the fake spectra caused by the SL and unable to be extracted precisely. Besides, when the frequency-coupling characteristic exists, FFD will also lead to a change in coupling frequencies. Thus, SL will also happen at the coupling frequencies, making it more difficult to extract measurement signals. Targeting this issue, this article analyzes the mechanism of SL and grasps the characteristics of fake spectra caused by SL. Accordingly, a Hann-window-based method is proposed to accurately extract the measurement signals during FFD. The superiority of the proposed method is none of the requirements to extend the original measurement time. Finally, the experiments based on control-hardware-in-loop are carried out to verify the effectiveness of the proposed method.**

***Index Terms*—Frequency coupling, fundamental frequency deviation (FFD), Hann window (HW), impedance measurement, spectral leakage (SL).**

I. Introduction

As THE utilization of renewable energy increases, the renewable power generator (RPG) based on power electronic technology has been extensively applied for the generation and delivery of renewable energy, which also produces instability risk to the renewable energy system [1], [2]. The instability risk is mainly caused by the insufficient stability margin of the interconnected system composed of the RPG and power grid. To mitigate the stability problem, stability analysis is necessary to analyze the stability of the system. Impedance-based stability analysis is a reliable method to judge the stability of interconnected systems [3], [4], [5], [6], in which the impedance models of the RPG and power grid are important information [7], [8], [9], [10].

Research studies on the impedance modeling of RPG have been widely reported in [5], [6], [7], [8], and [9]. In [5], [6], and [7], the impedance model of RPG is considered a single-input single-output model. The impedance model can be divided into positive- and negative-sequence models, which can be analyzed independently. However, the investigation presented in [8] and [9] reveals that the frequency-coupling characteristic exists in RPG, which is mainly due to the asymmetrical control [8], [9]. Assuming that f_1 is the fundamental frequency, the frequency-coupling characteristic is manifested in that while injecting the perturbation signal at the frequency of f_p Hz, the responses at f_p Hz and $(f_p - 2f_1)$ Hz will exist in the system simultaneously. Hence, the impedance characteristic will be characterized as a 2×2 matrix, in which the diagonal elements denote the positive- and negative-sequence impedance while the off-diagonal elements can reflect the degree of frequency-coupling characteristics [8]. The frequency-coupling characteristic should be considered while acquiring the impedance model of RPG; otherwise, incorrect stability analysis results may be obtained [8].

Impedance measurement is an effective method to obtain the impedance characteristic by injecting small-signal perturbations [10], [11], [12], [13], [14]. And then, the impedance can be calculated based on the terminal information [15], [16], [17], [18]. For example, maximum-length binary sequence and discrete-interval binary sequence are adopted in [12] and [13] to measure the grid impedance for adaptive control, gain scheduling, and reactive power control of grid-connected inverters. Additionally, a pseudorandom sequence is proposed to identify the battery impedance for health monitoring [14], [15], [16], [17]. Furthermore, orthogonal sequences are applied in [18] to measure the bus impedance of multiple interconnected inverters. Besides, the chirp signal is used in [19] and [20] to

Manuscript received 11 September 2022; revised 27 December 2022; accepted 29 January 2023. Date of publication 2 February 2023; date of current version 10 March 2023. This work was supported by the National Natural Science Foundation of China under Grant 51977194. Recommended for publication by Associate Editor G.-S Seo. *(Corresponding author: Heng Nian.)*

The authors are with the College of Electrical Engineering, Zhejiang University, Hangzhou 310027, China (e-mail: 11910042@zju.edu.cn; nianheng@zju.edu.cn; 12110058@zju.edu.cn; 11810031@zju.edu.cn; 11910049@zju.edu.cn; lihaipan@zju.edu.cn; 22010151@zju.edu.cn; 22110042@zju.edu.cn).

Color versions of one or more figures in this article are available at https://doi.org/10.1109/TPEL.2023.3241608.

Digital Object Identifier 10.1109/TPEL.2023.3241608

measure the impedance of a single-phase railway traction power system.

The above-mentioned research studies have greatly contributed to the improvement of impedance measurement techniques. Merely, the frequency-coupling characteristic is not considered in the above-mentioned methods, which is extensively observed in RPG [8], [9]. While considering the frequency-coupling characteristic in the measurement, two groups of linear-independent perturbation injection will be needed, and the perturbations and responses at f_p Hz and (f_p-2f_1) Hz should be obtained for calculating elements of the 2×2 matrix. The related research work has been widely discussed in [22], where a multisine signal is designed for obtaining accurate frequency-coupling characteristics of RPG.

However, the grid that is connected with the RPG may suffer frequency deviation from the fundamental frequency point [23], [24], which will bring difficulty to the impedance measurement considering the frequency-coupling characteristic

1) When fundamental frequency deviation (FFD) occurs, the frequency resolution of the discrete Fourier transformation (DFT) may be insufficient and thus spectral leakage (SL) occurs. Then, the fake spectra caused by the SL of the fundamental signal will be broadly spread in the frequency band and superimposed with the perturbations and responses, which will make it incapable of extracting these measurement signals for impedance calculation.
2) Due to the variation in the fundamental frequency, the coupling frequency $(f_p - 2f_1)$ Hz will also be changed [22]. Therefore, based on the same reason, SL will also occur at these coupling frequencies, and the measurement signals at $(f_p - 2f_1)$ Hz will be unable to be extracted precisely.

Selecting an appropriate sampling time and a reasonable frequency resolution for DFT can tackle the difficulty of signal extraction. However, since the deviation in frequency is uncertain, it is difficult to always select the optimal length of sampling. Extending the sampling time can reduce the extraction error of signals at $(f_p - 2f_1)$ Hz, which will considerably lower the measurement efficiency. Thus, it is a better choice to investigate the method to accurately extract the measurement signals under FFD without the requirement to extend measurement time.

In existing research, the impedance measurement during FFD has been studied in [23] and [24]. Zhong et al. [23] proposed a two-stage series multiple-complex coefficient filter (TSMCCF) to extract perturbations rapidly and precisely. This method is useful when a few frequencies with a large frequency interval are measured. Since the TSMCCF needs to be designed individually against each frequency component, when the measurement frequencies are plenty, the same number of TSMCCF should be designed. Moreover, when the perturbation frequencies are changed, the coefficients of TSMCCF also need to be adjusted correspondingly. Therefore, this method lacks flexibility. Furthermore, due to the fact that the magnitude of TSMCCF is not absolutely zero at a frequency close to the perturbation frequency, the extraction accuracy will be influenced when the frequencies of the two perturbations are close. Thus in [23], a relatively large frequency interval (100 Hz) is used, which is not small enough to measure the detailed impedance characteristic. The cascaded delayed signal cancellation (CDSC)-based method proposed in [24] also has the problem of low flexibility. Meanwhile, the CDSC-based method also only allows a few frequencies with a large interval. Finally, the frequency-coupling characteristic is not taken into account in the above-mentioned research, and thus the difficulty of extracting the signals at $(f_p - 2f_1)$ Hz when SL occurs has not been tackled so far.

In order to obtain the frequency-coupling characteristic of RPG under FFD, this article proposes a method that can extract perturbation signals precisely even when SL occurs without the requirement to extend the length of the sampling signal. This article analyzes the factors that determine the amplitude/phase–frequency characteristics of the fake spectra caused by SL. Accordingly, the method to estimate the real frequencies, amplitudes, and phases of measurement signals according to the information about the fake spectra is proposed. Furthermore, in order to minimize the mutual interference between adjacent perturbation signals while a wideband signal is used, the Hann window (HW) [25] is adopted to optimize this method. When FFD occurs, the proposed method can precisely extract the measurement signals at coupling frequencies, which is essential to obtain accurate measurement results of the frequency-coupling characteristic.

The rest of this article is organized as follows. Section II indicates the impact of FFD on measuring the frequency-coupling characteristic and the reason of poor measurement accuracy. In Section III, the mechanism of DFT and SL is analyzed, according to which the method of accurately extracting signals while SL occurs is proposed. Accordingly, the application of the proposed method to measure the frequency-coupling characteristic is introduced. In Section IV, experiments based on the Typhoon control-hardware-in-loop (CHIL) platform are carried out to validate the effectiveness of the proposed signal extraction method. Finally, Section V concludes this article.

II. Impact of FFD on Measuring the Frequency-Coupling Characteristic

Commonly, the frequency-coupling characteristic of the RPG can be depicted by a 2×2 admittance matrix. In order to achieve the measurement of the frequency-coupling admittance matrix, two groups of linearly independent perturbation signals are required [22].

In the process of the measurement, the following signals need to be obtained [8], [22]:

$$\begin{cases} V_s = \begin{bmatrix} \boldsymbol{V}_p[f_p] & \boldsymbol{V}_n[f_p] \\ \boldsymbol{V}_{p2}[f_p - 2f_1] & \boldsymbol{V}_{n2}[f_p - 2f_1] \end{bmatrix} \\ I_s = \begin{bmatrix} \boldsymbol{I}_p[f_p] & \boldsymbol{I}_n[f_p] \\ \boldsymbol{I}_{p2}[f_p - 2f_1] & \boldsymbol{I}_{n2}[f_p - 2f_1] \end{bmatrix} \end{cases} \tag{1}$$

where f_1 denotes the fundamental frequency; f_p denotes the frequency of the positive-sequence perturbation (PSP); $\boldsymbol{V}_s$ denotes the matrix containing the voltage measurement signal; $\boldsymbol{I}_s$ denotes the matrix containing the current measurement signal; $\boldsymbol{V}_p[f_p]$ and $\boldsymbol{V}_{p2}[f_p - 2f_1]$ represent the voltage signals at frequencies of f_p Hz and $(f_p - 2f_1)$ Hz, respectively, obtained in the first injection; $\boldsymbol{I}_p[f_p]$ and $\boldsymbol{I}_{p2}[f_p - 2f_1]$ represent the current signals at frequencies of f_p Hz and $(f_p - 2f_1)$ Hz, respectively, obtained in the first injection. $\boldsymbol{V}_n[f_p]$, $\boldsymbol{V}_{n2}[f_p - 2f_1]$, $\boldsymbol{I}_n[f_p]$, and

TABLE I
PARAMETERS OF THE TYPE-IV WT UNDER TEST

Parameter	Value	Parameter	Value
Rated voltage U_s	690 V	Filter inductance L	0.53 p.u.
Rated power P_s	1.5 MW	Stator Resistance R_s	0.004 p.u.
Fundamental frequency f_1	50.1 Hz	Rated Rotor Frequency f_r	7 Hz
Switching frequency f_s	5 kHz	GSC PLL control k_{pp}, k_{pi}	44 500 p.u.
Pole Pairs n_p	5.2 p.u.	GSC current control k_{ip}, k_{ii}	3.35 315 p.u.
Magnetic Flux φ_m	8.15 Wb	GSC voltage control k_{vp}, k_{vi}	1.56 55 p.u.
Stator Inductance L_{sd}, L_{sq}	2.1 3.1 p.u.	Dc-link voltage V_{dc}	1200 V
DC capacitance C_{dc}	5.2 p.u.	MSC current control k_{sip}, k_{sii}	9.8 612 p.u.

$\boldsymbol{I}_{n2}[f_p - 2f_1]$ represent the measurement signals obtained in the second injection. The admittance matrix that describes the frequency-coupling characteristic can be obtained by (2). Note that the frequency is omitted for simplicity [22]

$$\begin{bmatrix} Y_{11} & Y_{12} \\ Y_{21} & Y_{22} \end{bmatrix} = \begin{bmatrix} I_p & I_n \\ I_{p2} & I_{n2} \end{bmatrix} \begin{bmatrix} V_p & V_n \\ V_{p2} & V_{n2} \end{bmatrix}^{-1}. \quad (2)$$

Normally, the fundamental frequency is certain and known before the impedance measurement, and thus the values of f_p and $(f_p - 2f_1)$ are easy to acquire. And DFT with sufficient frequency resolution can be utilized to extract the amplitudes and phases of the measurement signals in (1). Accordingly, elements of the admittance matrix can be calculated by (1). Single sine-signal and multisine signal injection can both be adopted for the above-mentioned process. For avoiding the mutual interference brought about by frequency coupling, frequency bins of the multisine signal should be designed properly [22].

However, the deviation of f_1 may occur [23], [24] and will cause a change in the coupling frequency $(f_p - 2f_1)$. If the deviation is smaller than the original frequency resolution, the frequency resolution is likely to be insufficient to accurately extract the measurement signals. As a result, SL will occur, which will result in the following two challenges.

1) The SL of the fundamental signal will lead to the appearance of fake spectra in a wide frequency band, which will interfere with the precise extraction of measurement signals.
2) It is difficult to obtain the signals at $(f_p - 2f_1)$ Hz due to the insufficient frequency resolution. Moreover, when multiple perturbation signals are injected at one time, the fake spectra caused by the SL of the signals at $(f_p - 2f_1)$ Hz may be superimposed with the adjacent frequency components and make it more difficult to extract measurement signals precisely.

In the rest of Section II, the experiments based on the Typhoon CHIL platform will be carried out to reveal the issue. A detailed description of the platform is presented in Section IV. The measurements for Y_{11} and Y_{21} of a type-IV wind turbine (WT) will be given. The parameters are presented in Table I. In this case, $f_1 = 50.1$ Hz.

In this case, 18 integer measurement frequencies in the 10–1000 Hz range are set for Y_{11} and 15 integer measurement frequencies in the 10–200 Hz range are set for Y_{21}. Since the magnitude of Y_{21} in the 200–1000 Hz range is extremely small,

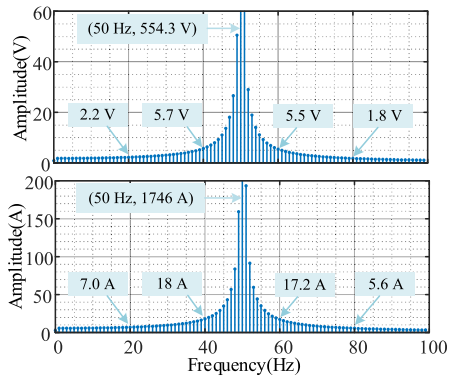

Fig. 1. DFT results of voltage and current signals in phase a.

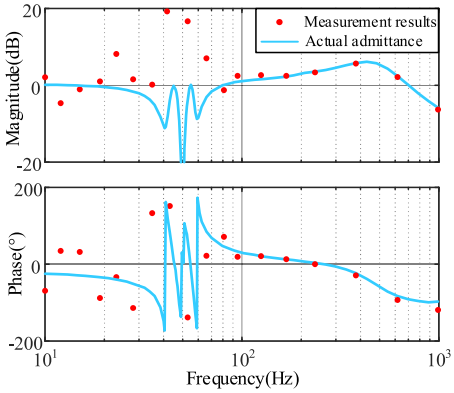

Fig. 2. Measurement results for Y_{11}.

the admittance in this frequency band will not be measured. The multisine signal is adopted as the perturbation signal due to the better control ability of the spectrum characteristic [10]. After injecting the multisine signal, the waveforms of voltages and currents at the terminal of type-IV WT in 1 s are sampled for calculating Y_{11} and Y_{21}, and the frequency resolution is 1 Hz. The DFT results for the voltage and current in phase a are shown in Fig. 1. As shown in Fig. 1, since the frequency resolution is not enough to extract the fundamental signal at 50.1 Hz, SL occurs, and the fake spectra appear in a wide frequency band. Note that the amplitudes of fake spectra are relatively high compared with the measurement signals in a wide frequency span, which will certainly impact the accurate extraction of measurement signals. A similar SL will also appear in the adjacent frequency bands of the measurement signals at $(f_p - 2f_1)$ Hz, which will encumber the extraction of these signals.

The measurement results of Y_{11} and Y_{21} are shown in Figs. 2 and 3, respectively, in which the blue solid lines denote the actual admittance curves obtained by frequency scans based on the injection of a single-sine signal [26]. Since the use of a single-sine signal has the highest signal-to-noise ratio (SNR), the results obtained by the frequency scan are considered accurate admittance [10]. According to the figures, the largest measurement error of Y_{11} can reach 26 dB and 157°, whereas the largest

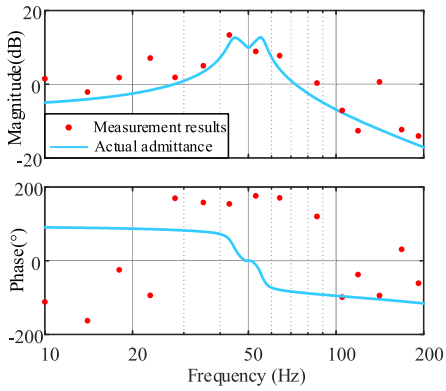

Fig. 3. Measurement results for Y_{21}.

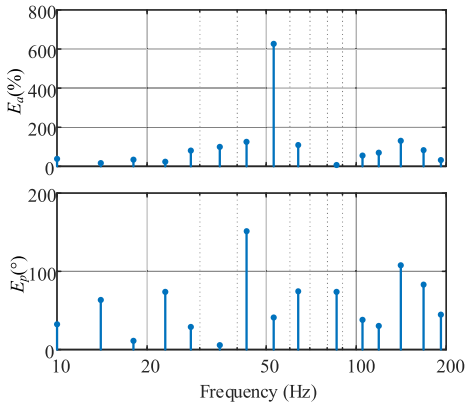

Fig. 5. Extraction error of $\boldsymbol{I}_{p2}[f_p - 2f_1]$ while measuring Y_{21}.

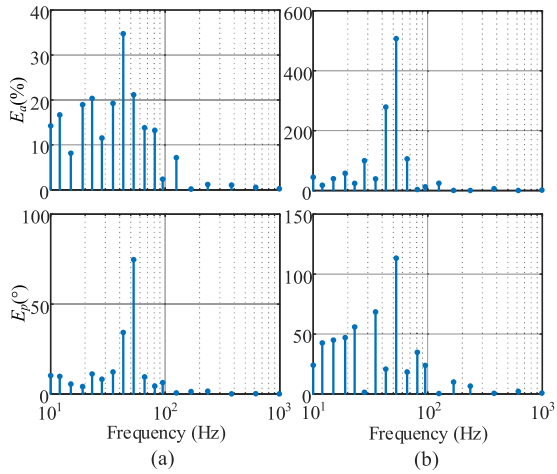

Fig. 4. Extraction errors of (a) $\boldsymbol{V}_p[f_p]$ and (b) $\boldsymbol{I}_p[f_p]$ while measuring Y_{11}.

measurement error of Y_{21} can reach 12 dB and 171°, indicating poor measurement accuracy.

From the measurement results of Y_{11}, it can be seen that the accuracy around f_1 (10–100 Hz) is much worse than that in the frequency band far away from f_1 (100–1000 Hz). Combining the content shown in Fig. 1, since the amplitudes of the fake spectra are larger in the 10–100 Hz range, the impact of SL on the extraction precision of measurement signals in the 10–100 Hz range is more serious than that in the 100–1000 Hz range. Note that the main signals that are used for calculating Y_{11} are $\boldsymbol{V}_p[f_p]$ and $\boldsymbol{I}_p[f_p]$ [22]. Since $\boldsymbol{V}_p[f_p]$ and $\boldsymbol{I}_p[f_p]$ can be extracted directly by DFT based on the 1-s sampling signal, the SL of fundamental signals is the only factor that may impact the accurate extraction of $\boldsymbol{V}_p[f_p]$ and $\boldsymbol{I}_p[f_p]$. Thereby, the frequency components that are far away from f_1 can be extracted more accurately, whereas the frequency components near f_1 will be extracted with low precision.

In order to corroborate the above-mentioned analysis, the extraction errors of $\boldsymbol{V}_p[f_p]$ and $\boldsymbol{I}_p[f_p]$ are depicted in Fig. 4, in which $E_a(\%)$ denotes the relative error of amplitude and $E_p(°)$ denotes the phase error.

It can be concluded that the extraction error is great, especially in the10–100 Hz range, whereas the error is small in the 100–1000 Hz range. Consequently, the measurement error of Y_{11} is greater in the 10–100 Hz range, which is consistent with the analysis.

The main signals that are used to calculate Y_{21} are $\boldsymbol{I}_{p2}[f_p - 2f_1]$ and $\boldsymbol{V}_p[f_p]$ [22]. The extraction of $\boldsymbol{I}_{p2}[f_p - 2f_1]$ is not only influenced by the SL of fundamental signals but also by the SL of themselves ($\boldsymbol{I}_{p2}[f_p - 2f_1]$). The extraction error of $\boldsymbol{I}_{p2}[f_p - 2f_1]$ is shown in Fig. 5. As shown in the figure, the extraction error is considerable in the 10–200 Hz range. Thus, the measurement accuracy is poor in the whole concerned frequency band.

According to the above-mentioned cases, when FFD occurs, the impact from the SL of the fundamental signal should be eliminated, and the extraction method of signals at $(f_p - 2f_1)$ Hz needs to be investigated, so as to obtain precise measurement results. Apparently, extending the length of sampling to acquire higher frequency resolution will be useful; however, the measurement efficiency will be jeopardized. Therefore, the method without the requirement to extend the measurement time should be researched.

III. Extraction Method of Frequency Components Under SL

A. Analysis on the Mechanism of SL

For the sake of investigating the method to extract measurement signals without extending the length of sampling, it is required to have the ability to estimate the real frequencies, amplitudes, and phases of measurement signals according to the spectrum with SL. Therefore, the mechanism and characteristics of SL should be analyzed.

DFT is a common method to extract the spectral characteristics of time-domain signals. In the impedance measurement, DFT is often used to extract the perturbation components from the voltage and current signals for impedance calculation. In order to study the characteristics of SL when the frequency resolution is insufficient, it is necessary to analyze the cause of SL combined with the principle of DFT.

First, taking the signal with a frequency of f_0 Hz as an example, the discrete time-domain sequence $x(n)$ can be obtained by long-time sampling [27], [28], [29]

$$x(n) = \cos\left(2\pi f_0 \frac{n}{f_s}\right), n = 0, 1, 2, \ldots \tag{3}$$

where f_s is the sampling rate.

Second, before implementing DFT, a window function will be selected to extract a group of finite-length sequences from $x(n)$, which is defined as $x_N(n)$. Generally, the rectangular window (RW) is usually used. The time-domain expression of an RW is given as follows [27], [28], [29]:

$$w(n) = R(n) = \begin{cases} 1, 0 \le n \le N-1 \\ 0, n > N-1 \end{cases} \tag{4}$$

where $w(n)$ denotes the time-domain window function, $R(n)$ denotes the time-domain function of RW, and N is the length of $x_N(n)$. The expression of $x_N(n)$ is given as follows:

$$x_N(n) = w(n)x(n) = R(n)x(n). \tag{5}$$

The spectrum characteristic of $x_N(n)$ will be different from that of $x(n)$. According to (5), the spectrum characteristic of $x_N(n)$ can be written as follows:

$$X_W(e^{j\omega}) = \frac{1}{2\pi} X(e^{j\omega}) \otimes W_R(e^{j\omega}) \tag{6}$$

where $W_R(e^{j\omega})$ represents the frequency-domain expression of the RW and is expressed as follows [27], [28], [29]:

$$W_R(e^{j\omega}) = \sum_{n=0}^{N-1} R(n)e^{-j\omega n} = e^{-j\omega\frac{N-1}{2}} \frac{\sin(\omega N/2)}{\sin(\omega/2)}. \tag{7}$$

$X(e^{j\omega})$ is the frequency-domain expression of $x(n)$ and is given as follows:

$$X(e^{j\omega}) = \pi[\delta(\omega - \omega_0) + \delta(\omega + \omega_0)] \tag{8}$$

where $\omega_0 = 2\pi f_0$.

Accordingly

$$X_W(e^{j\omega}) = \frac{1}{2}[W_R(e^{j(\omega-\omega_0)}) + W_R(e^{j(\omega+\omega_0)})]. \tag{9}$$

According to (9), the windowing operation on $x(n)$ is equivalent to shifting the spectral characteristics of the window function to the left and right by f_0 Hz and superimposing them with each other. For example, when $f_0 = 5$ Hz, $N = 10\,000$, and $f_s = 10\,000$ Hz, the frequency-domain characteristics of $X_W(e^{j\omega})$ are shown in Fig. 6. As shown in Fig. 6, the interval between two adjacent zero points of the amplitude–frequency curve is $f_s/N = 1$ Hz.

Third, DFT will be employed on $x_N(n)$ so as to estimate the spectrum characteristic of $x(n)$. In the frequency domain, DFT is equivalent to sampling $X_W(e^{j\omega})$ at f_s/M Hz intervals, where M is the number of points utilized for DFT [27], [28], [29]. f_s/M can be defined as the frequency resolution (f_r) of DFT. The DFT results for $f_0 = 5$ Hz and $M = N = 10\,000$ are given in Fig. 7.

Since $N = M$, the sampling position of DFT is just at the zero points and the maximum point of the amplitude–frequency curve for $X_W(e^{j\omega})$, so that the accurate spectrum characteristic of $x(n)$ can be obtained. In the following, when $M = 1.02N = 10\,200$, the DFT results are shown in Fig. 8. Because $f_r \approx 0.98$ Hz, the sampling position is no longer only at the zero points and the maximum point; thus, many spectral lines that are not equal to zero, which is the SL phenomenon. Therefore, the DFT results fail to reflect the real spectrum of $x(n)$.

In this case, since $M > N$, the number of points used for DFT is more than the length of $x_N(n)$. Thereby, zeros will be added at the end of $x_N(n)$ until the points are enough. According to the results presented in Fig. 8, zero-adding will lead to SL and inaccurate spectrum estimation.

In another condition, if $f_0 = 55.3$ Hz and $M = N$, the DFT results will be performed as shown in Fig. 9.

As shown in Fig. 9, since $f_r = 1$ Hz, the spectral lines are all at integer frequencies, making the component at 55.3Hz unable to be extracted precisely. SL occurs, and in the adjacent frequency band of 55.3 Hz, the fake spectra that gradually decay away from 55.3 Hz are generated. According to this case, another condition

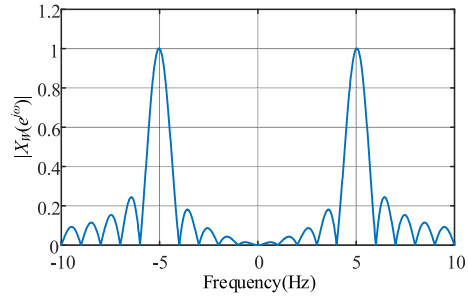

Fig. 6. Amplitude–frequency characteristic of $x_N(n)$.

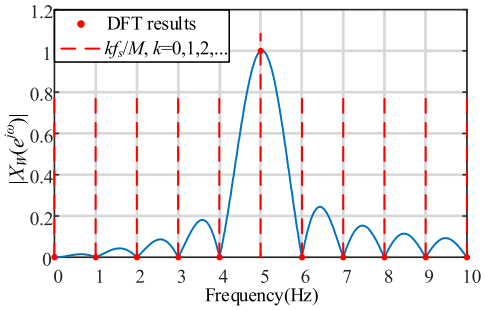

Fig. 7. DFT results when $f_0 = 5$ Hz and $M = N$.

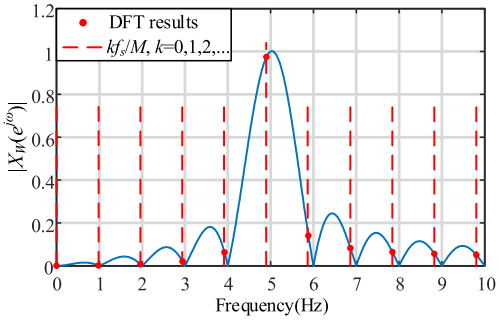

Fig. 8. DFT results when $f_0 = 5$ Hz and $M = 1.02N$.

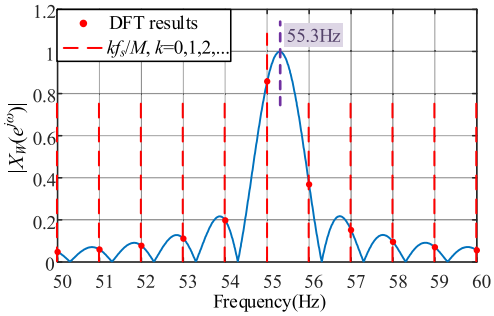

Fig. 9. DFT results when $f_0 = 55.3$ Hz and $M = N$.

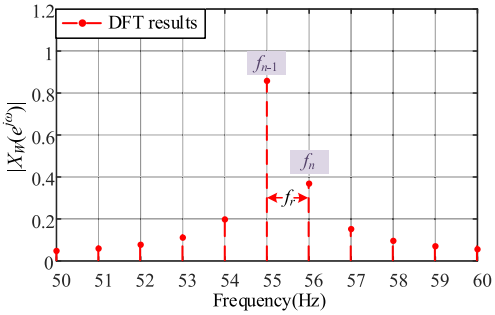

Fig. 10. Schematic for choosing f_n and f_{n-1}.

that will lead to SL is the insufficiency of f_r. Furthermore, the characteristics of the fake spectra generated by SL will be dependent on the minimum distance between the real frequency and kf_r ($k = 0, 1, 2, \ldots$) and the spectrum characteristic of the window function. This insufficient f_r is caused by the insufficient sampling signal length, which is also the reason for the poor accuracy shown in Figs. 2 and 3.

B. Extraction Method of the Frequency Components

Based on the above-mentioned analysis, it is known that the characteristic of fake spectra is determined by the window function and the distance between the real frequency and f_r. Therefore, the real frequency, amplitude, and phase of the signal can be estimated according to the amplitude–frequency characteristic of fake spectra. The following procedure can be employed to extract the signals at the frequencies where SL occurs.

1) The frequencies, amplitudes, and phases of the two nearest fake spectra are, respectively, defined as f_n, a_n, p_n and f_{n-1}, a_{n-1}, p_{n-1}. Moreover, $f_n - f_{n-1} = f_r$. Take the case when $f_0 = 55.3$ Hz and $M = N$ as an example, f_n and f_{n-1} will be given as shown in Fig. 10.

The amplitude ratio of the nearest two spectra ($R_1 = a_n/a_{n-1}$) is acquired, which will be compared with the amplitude–frequency curve of the frequency-domain window function so as to judge the distance between the real frequency and the nearest spectral lines.

Fig. 11 depicts the specific procedure for this step. In the figure, the blue solid line denotes the magnitude of $W_R(e^{j\omega})$.

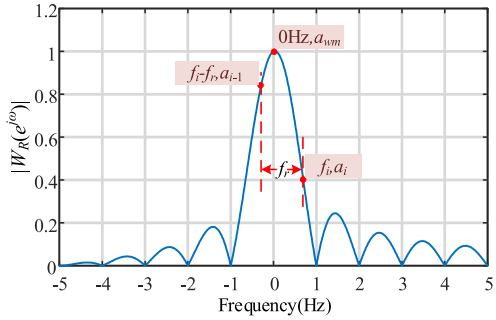

Fig. 11. Schematic for the procedure of estimating f_t.

First, f_i can be selected from 0 to f_r Hz at one certain interval, according to which the magnitude of $W_R(e^{j\omega})$ at f_i Hz (a_i), f_i–f_r, and the magnitude of $W_R(e^{j\omega})$ at (f_i–f_r) Hz (a_{i-1}) can be obtained. Second, $R_2 = a_i/a_{i-1}$. As f_i varies from 0 to f_r, when $R_2 = R_1$, the real frequency of the signal (f_t) can be determined by

$$f_t = f_n - f_i. \tag{10}$$

According to this step, f_t can be estimated. The reason of choosing the nearest spectral lines is that the nearest spectra have the highest amplitudes, which suffer the least noise and harmonic interference.

1) After determining the real frequency, the amplitude and phase of the signal can be further derived according to the amplitudes and phases of the nearest fake spectra. Assuming that the frequency, amplitude, and phase of the nearest spectral line are f_{near}, a_{near}, and p_{near}, respectively; the real amplitude and phase of the signal at f_t Hz are a_t and p_t, respectively; the amplitude and phase of $W_R(e^{j\omega})$ at 0 Hz are a_{wm} and p_{wm}, respectively; the amplitude and phase of $W_R(e^{j\omega})$ at (f_{near}–f_r) Hz are a_w and p_w, respectively. And then, a_t and p_t can be expressed as follows:

$$a_t = \frac{a_{\text{near}} a_{wm}}{a_w}, p_t = p_{\text{near}} + p_{wm} - p_w. \tag{11}$$

C. Selection of Windows

The proposed method can estimate the real frequency, amplitude, and phase of the signal according to the characteristics of the nearest fake spectra. When a wideband signal is adopted, multiple harmonics will be injected at one time. The superimposition of fake spectra from different harmonics may occur, which will interfere with the accuracy of the extracted signals. Therefore, the amplitudes of the fake spectra should be attenuated quickly to avoid mutual interference. The attenuation rate of the fake spectra is only related to the window function. In the following, the spectrum characteristics of several representative windows, including RW, HW, and Hamming window (HMW), are compared to select the optimal window.

The time-domain function of HW is written as follows [25]:

$$H(n) = 0.5\left[1 - \cos\left(\frac{2\pi n}{N}\right)\right], 0 \le n \le N-1. \tag{12}$$

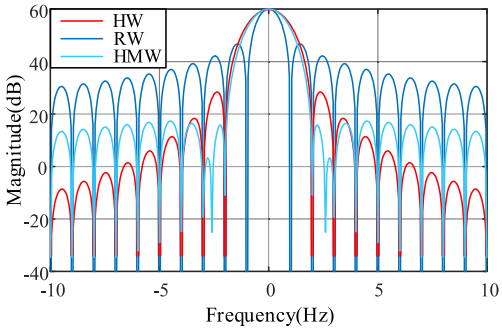

Fig. 12. Amplitude–frequency curves of HW, HMW, and RW.

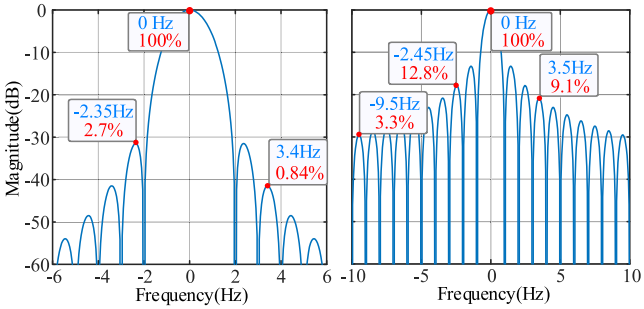

Fig. 13. Spectrum comparison of HW and RW (left: HW; right: RW).

According to (12), the frequency-domain expression of $H(n)$ can be derived as follows:

$$W_H(\omega) = \sum_{n=0}^{N-1} H(n)e^{-j\omega n} = \frac{\sin(\omega N/2)(q_1 + q_2 - q_3)}{e^{j\omega N/2}} \tag{13}$$

where

$$\begin{cases} q_1 = \frac{e^{j\omega/2}}{2\sin(\omega/2)} \\ q_2 = \frac{e^{j(\omega/2-\pi/N)}}{4\sin(\pi/N-\omega/2)} \\ q_3 = \frac{e^{-j(\omega/2-\pi/N)}}{4\sin(\pi/N+\omega/2)} \end{cases}. \tag{14}$$

Furthermore, the time-domain and frequency-domain expressions of HMW are represented as follows [28]:

$$w(n) = M(n) = 0.58 - 0.42\cos\left(\frac{2\pi n}{N}\right), 0 \le n \le N-1 \tag{15}$$

$$W_M(\omega) = \frac{\sin(\omega N/2)}{e^{j\omega N/2}}(1.16q_1 + 0.84q_2 - 0.84q_3). \tag{16}$$

According to (7), (13), and (16), the amplitude–frequency curves of RW, HW, and HMW are plotted in Fig. 12 [28].

According to Fig. 12, as the frequency gradually moves away from 0 Hz, the magnitude decreases gradually. Among them, HW obviously has the fastest descending rate, whereas RW has the slowest descending rate. In order to highlight the difference, the comparison between the amplitude–frequency characteristics of RW and HW is depicted in Fig. 13.

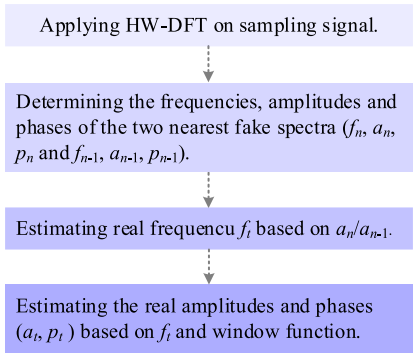

Fig. 14. Flowchart of the proposed method to extract perturbation components.

From Fig. 13, it can be observed that at 2–3 Hz, the largest value of the fake spectra using HW can be decreased to 2.7%. For comparison, while using RW at 2–3 Hz, the largest amplitude is 12.8%, which is much larger than that while using HW. And 12.8% still have the risk of interfering with the estimation of other signals. The magnitude of the frequency-domain expression of RW at 9.5 Hz is 3.3%, which is still slightly worse than 2.7%. Therefore, using HW can minimize the interference of different harmonics and allow much smaller intervals between measurement frequencies.

Overall, the flowchart of the proposed method to extract perturbation components is presented in Fig. 14.

D. Measuring the Frequency-Coupling Characteristic Using the Proposed Method

The extraction method for the measurement signals at $(f_p - 2f_1)$ Hz during FFD is proposed in Section III-C. In the following, the application scheme of the proposed signal extraction method for measuring the frequency-coupling characteristic will be introduced.

1) Fundamental Signal Extraction and Subtraction: When the fundamental frequency deviates, the original frequency resolution may be insufficient to extract the fundamental signal, and thereby SL will occur, and the fake spectra will be great in a wide frequency band. Therefore, after sampling the voltage and current signals at the terminal of RPG, the fundamental signal should be extracted by the proposed method to obtain the frequency (f_g), amplitude (A_g), and phase (P_g) of the fundamental signals. Accordingly, for the sake of eliminating the influence of the fundamental signal, the fundamental signal will be reconstructed in time domain and subtracted from the original sampling signal. The reconstructed signal can be calculated as follows:

$$F(n) = A_g \cos\left(2\pi f_g \frac{n}{f_s} + P_g\right), n = 0, 1, 2, \ldots, N-1. \tag{17}$$

2) Measurement Signal Extraction: $\boldsymbol{V}_p[f_p]$, $\boldsymbol{V}_n[f_p]$, $\boldsymbol{I}_p[f_p]$, and $\boldsymbol{I}_n[f_p]$ can be directly obtained by DFT using RW. And then, $\boldsymbol{V}_{p2}[f_p - 2f_1]$, $\boldsymbol{V}_{n2}[f_p - 2f_1]$, $\boldsymbol{I}_{p2}[f_p - 2f_1]$, and $\boldsymbol{I}_{n2}[f_p - 2f_1]$ will be extracted by the proposed signal extraction method. To minimize the mutual interference due to the injection of multiple

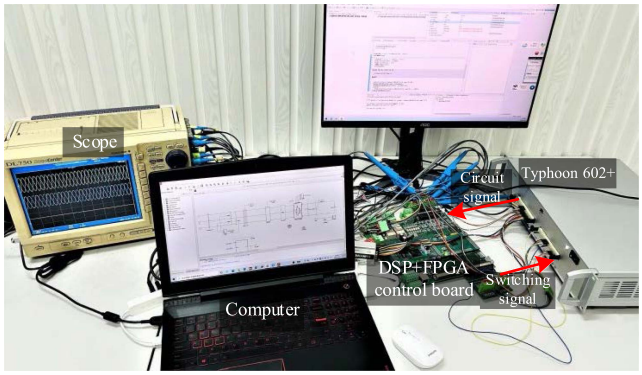

Fig. 15. Hardware platform of the CHIL experiment.

harmonics, HW is utilized. This method will be named the HW-DFT-based method in the following.

3) Impedance Calculation: Based on the extracted measurement signal, the elements of the admittance matrix that can describe the frequency-coupling characteristic can be calculated by (2).

IV. Experimental Verification

A. Introduction of the CHIL Platform

For validating the effectiveness of the proposed HW-DFT-based method, the experiments based on CHIL are carried out. In the experiments, the impedance characteristic of a type-IV WT is measured by the proposed method. The parameters of the type-IV WT are given in Table I. The hardware platform of the CHIL experiment is shown in Fig. 15. For the emulation of the practical operation condition of the high-power RPG, the model of the MW-level type-IV WT is developed in Typhoon 602+ with the time step of 1 μs. Controllers of the type-IV WT are executed in a TMS320F28335/Spartan 6 XC6SLX16 DSP+ FPGA control board, and the sampling frequency is set at 5 kHz. There are signal conditioning circuits on the control board. Using an analog/digital converter (ADC), the circuit signals can be sampled by the control board and then utilized for the generation of the switching signal, which can be outputted by the digital output ports of the control board. Furthermore, by analog output ports and digital input ports, the Typhoon 602+ platform can implement the output of circuit signals and receive the switching signal from the control board. The sampling ADC of the control board adopts AD7606 of Analog Devices (ADI) Company. Accordingly, a 16-channel, 16-b ADC is constituted by two 8-channel, 16-b AD7606, and the analog input range of each is $\pm$20 V with overvoltage and overcurrent protection.

In this article, the impedance measurement system is shown in Fig. 16.

As shown in Fig. 16, the perturbation generator is connected in series with the type-IV WT. The function of the perturbation generator is to inject a small-signal perturbation signal while supplying operating voltage to the type-IV WT.

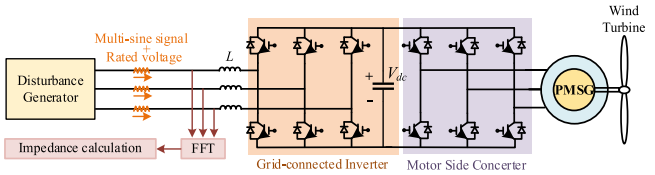

Fig. 16. Schematic of the impedance measurement system.

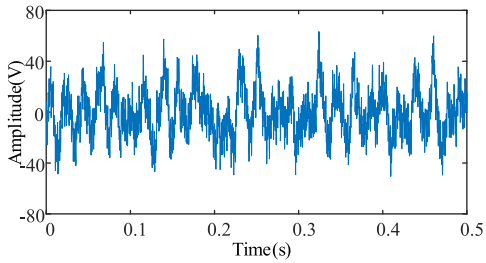

Fig. 17. Waveform of the injected multisine signal at phase a.

B. Implementation of the Proposed Method

The same as the case presented in Section II, Y_{11} at 18 integer measurement frequencies and Y_{21} at 15 integer measurement frequencies are measured by the proposed method to verify the effectiveness of the proposed method. The multisine signal is adopted as the perturbation signal [22]. The frequencies are [10, 12, 15, 19, 23, 28, 35, 43, 53, 66, 81, 95, 125, 168, 235, 379, 617, 991] Hz for Y_{11} and [10, 14, 18, 23, 28, 35, 43, 53, 64, 86, 105, 119, 141, 168, 192] Hz for Y_{21}. The amplitudes and phases of injected multisine signal are determined by the method presented in [10]. The waveform of the injected multisine signal at phase a is shown in Fig. 17.

During the perturbation injection, the waveforms of the three-phase line-to-line voltages at the point of common coupling (PCC) ($\boldsymbol{U}_{\mathrm{PCC}}$), output currents ($\boldsymbol{I}_{abc}$), and the output power (P_{o}, Q_{o}) of the type-IV WT are shown in Fig. 18. As shown in the figure, before the perturbation injection, the waveforms are standard three-phase sine waves, indicating the normal operation of the system. While injecting perturbation, the superimposition of the multisine signal causes the waveform distortion. When the injection is disabled, the waveforms can still return to standard three-phase sine waves, indicating the system is still operating normally.

First, Y_{11} is measured by the proposed method. The fundamental signals of voltage and current are extracted by the proposed method. The procedure is displayed in Fig. 19. As shown in Fig. 19(a), the amplitude ratio of the two nearest spectral lines is $R_1 = 279.1/161.5 \approx 1.728$. According to Fig. 19(b), the amplitude ratio of HW at -0.1 to 0.9 Hz is $0.4968/0.2876 \approx 1.727$, which is almost equal to R_1. Therefore, the real fundamental frequency $f_t = 50.1$ Hz. Then, according to the procedure introduced in Section III-B2 and Fig. 19, it can be determined that $f_{\mathrm{near}} = 50$ Hz, $a_{\mathrm{near}} = 279.1$ V, $p_{\mathrm{near}} = 169.7°$, $a_{wm} = 1$ pu, $p_{wm} = 0°$, $a_w = 0.4968$, and $p_w = 18°$. Based on (11), the real amplitude and phase of the fundamental signal can be derived.

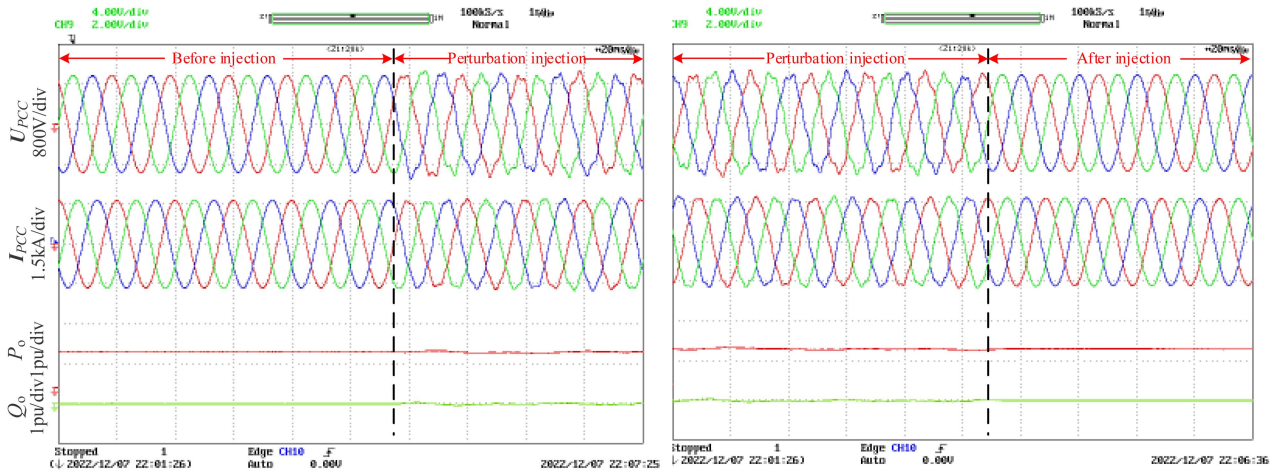

Fig. 18. Experimental waveforms of the voltages at PCC, output currents, and output power of the type-IV WT.

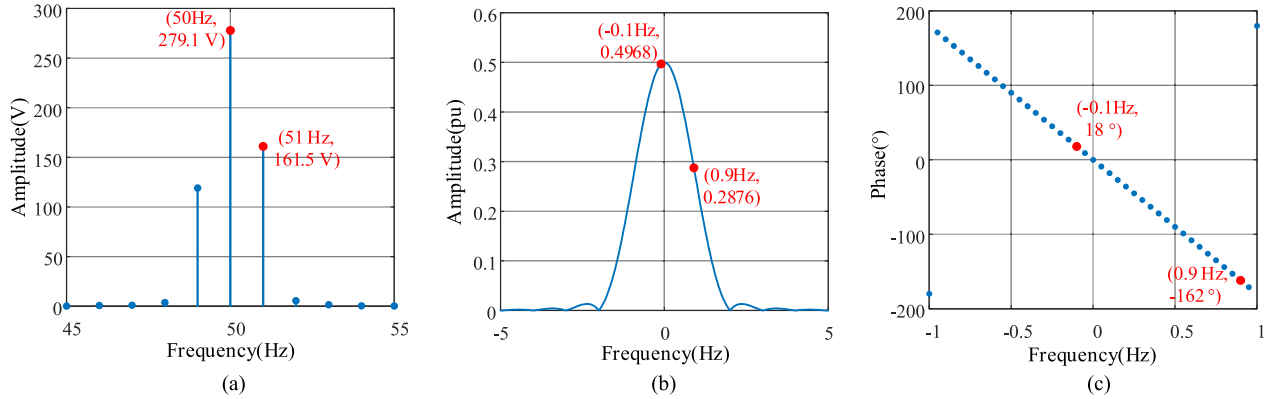

Fig. 19. Procedure of extracting fundamental signal. (a) HW-DFT results around the fundamental frequency. (b) Amplitude–frequency curve of HW. (c) Phase–frequency curve of HW.

In this way, the frequency, amplitude, and phase of the fundamental signal can be extracted by the proposed method based on 1-s sampling, which are respectively [561.94 V, 151.7°] for voltage and [1765.2 A, 150.9°] for current, whereas the real value obtained by DFT based on 10-s sampling is [561.75 V, 153.2°] for voltage and [1765.7 A, 152.5°] for current. It can be seen that the extracted value almost has no error compared to the real value, which validates the accuracy of the proposed method.

After extracting and subtracting the fundamental signal from the original sampling signals, the measurement signals can be further extracted by the proposed method. Fig. 20 shows the extraction error for the amplitudes of $\boldsymbol{V}_p[f_p]$ and $\boldsymbol{I}_p[f_p]$, which are named E_{va} and E_{ia}, respectively. According to the figure, E_{va} is all lower than 3%, whereas E_{ia} is all lower than 6%, which is accurate enough to obtain precise measurement results for Y_{11}, indicating that the fundamental signal has been accurately subtracted from the sampling signal and thereby the SL of the fundamental signal will not influence the extraction of measurement signals.

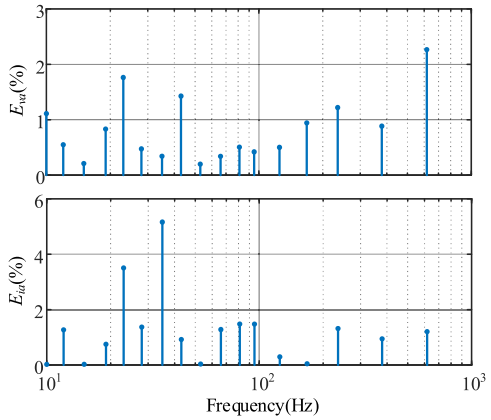

Fig. 20. Extraction error for the amplitude of $\boldsymbol{V}_p[f_p]$ and $\boldsymbol{I}_p[f_p]$.

The measurement results for Y_{11} are shown in Fig. 21(a). In the figure, the asterisks denote the results obtained by the proposed method, and the red dots denote the results obtained by DFT.

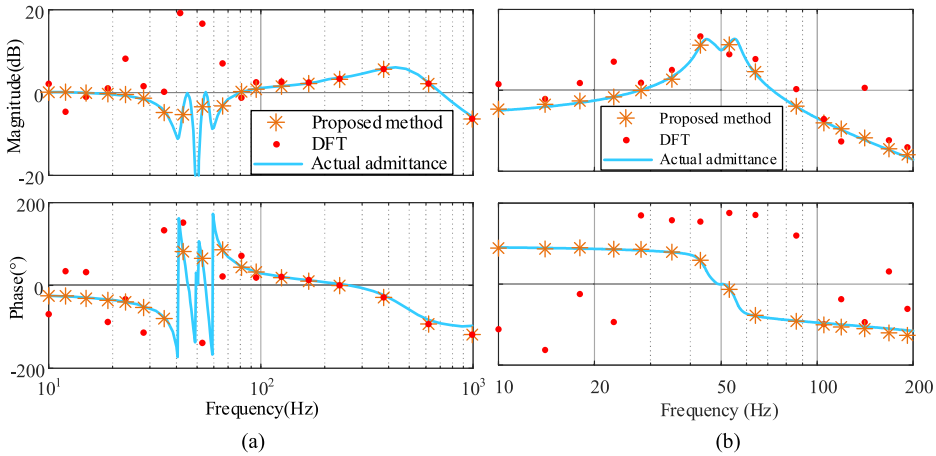

Fig. 21. (a) Measurement results of Y_{11}. (b) Measurement results of Y_{21}.

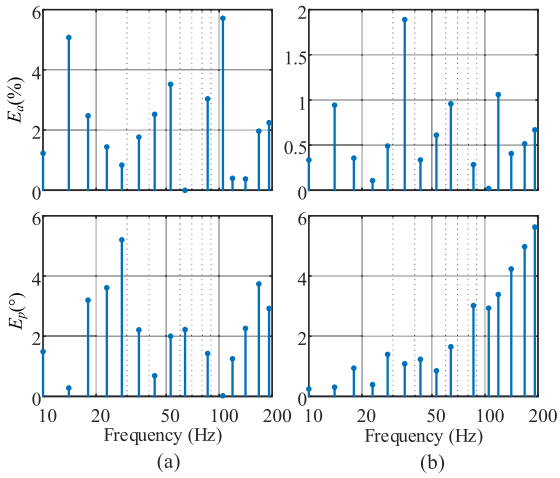

Fig. 22. Extraction error for $\boldsymbol{V}_p[f_p]$ and $\boldsymbol{I}_{p2}[f_p - 2f_1]$.

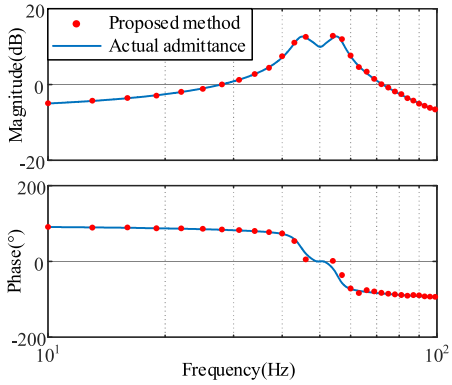

Fig. 23. Measurement results of Y_{21} at the interval of 3 Hz.

The length of the sampling signal remains 1 s while employing two methods. Besides, the actual admittance is obtained by a frequency scan based on the injection of a single-sine signal [26]. Since the asterisks coincide with the actual admittance curves, the accuracy of the results obtained by the proposed method can be concluded.

Second, Y_{21} is measured. The measurement signals at coupling frequencies are extracted by the proposed HW-DFT-based method. In order to reveal the accuracy of extracted signals, the errors of extracted signals are given in Fig. 22. According to the figure, the errors are lower than 6% and 6° for $\boldsymbol{I}_{p2}[f_p - 2f_1]$, and the errors are lower than 2% and 6° for $\boldsymbol{V}_p[f_p]$, revealing the precision of extracted signals.

The measurement results of Y_{21} are shown in Fig. 21(b). According to the figure, the red dots heavily deviate from the actual admittance, while the asterisks coincide with the actual admittance, revealing the accuracy of the measurement results obtained by the proposed method.

Subsequently, for the sake of testing the minimum allowed interval of measurement frequencies while applying the proposed method, the measurement of Y_{21} at an interval of 3 Hz in the 10–100 Hz range is conducted. The results are shown in Fig. 23.

According to Fig. 23, the measurement results coincide with the actual admittance curves, indicating that the proposed method can be effective while the frequency interval is only 3 Hz.

C. Comparison With the Existing Method

In order to clarify the superiority of the proposed method, the comparison between the proposed method and the existing method proposed in [24] is given. In [24], a CDSC-based method is proposed to accurately obtain the impedance of the measured system under adverse grid voltage conditions, including FFD.

By adjusting the parameters of CDSC, the unfavorable signals, such as unfavorable perturbations, the fundamental signal, and harmonics, can be eliminated by a group of CDSC. Finally, only the desired perturbations remain and can be separated by another group of CDSC. Note that only perturbations with the same frequency interval can be extracted by a group of CDSC, requiring that the measurement frequencies should have equal frequency intervals [24].

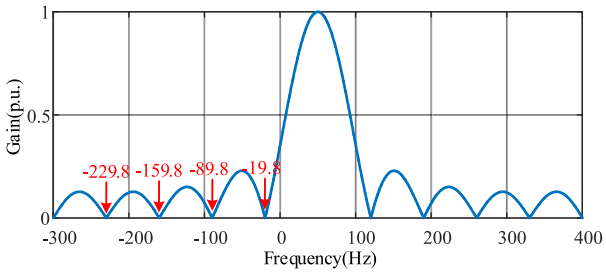

Fig. 24. Amplitude–frequency characteristic of the NSP-filter CDSC.

The main advantage of the CDSC method is that the time-domain waveform of a single perturbation can be extracted individually, and the amplitude and phase of the perturbation signal can be obtained based on the extracted waveform. Therefore, DFT is not required, and only several complete periods of the perturbation are enough to acquire useful information [24].

For illustration, a case is presented to reveal the performance of the CDSC-based method. According to the requirement of equal intervals, the frequencies are [120, 190, 260, 330] Hz. After injecting the perturbations at these frequencies and sampling the terminal signals of a type-IV wind turbine, the perturbations are required to be extracted by CDSC. The transfer function of a DSC can be written as follows:

$$\mathrm{DSC}_n^T(s) = \frac{1}{2}\left(1 + e^{\frac{(-s+j2\pi f_{\mathrm{tag}})T}{n}}\right). \tag{18}$$

In (18), f_{tag} denotes the rotation frequency, T is the delay period, and n is the delay coefficient.

Due to the frequency-coupling characteristic, the PSP at [120, 190, 260, 330] Hz and the negative-sequence perturbations (NSP) at [19.8, 89.8, 159.8, 229.8] Hz will be extracted. Since the main focus of this article is FFD, the elimination of harmonics and the fundamental signal will be considered perfect.

For PSP extraction, the NSP-filter CDSC is used to eliminate NSP. The transfer function of the CDSC is given as follows [24]:

$$\mathrm{CDSC}(s) = \mathrm{DSC}_2^T(s)\mathrm{DSC}_4^T(s)\mathrm{DSC}_8^T(s) \tag{19}$$

Since the first eliminated frequency is 19.8 Hz and the frequency interval (f_{int}) is 70 Hz, in (19), T = 1/70 s and $f_{\mathrm{tag}} = 70-19.8 = 50.2$ Hz. The amplitude–frequency characteristic of the NSP-filter CDSC is shown in Fig. 24.

As shown in Fig. 24, the gain of CDSC at NSP frequencies is zero to eliminate NSP, which refers to the red parts in the figure. In this way, theoretically, only PSP exists in the output signal. The next step is to separate the four PSPs. For example, the PSP separation CDSC with the amplitude–frequency characteristic in Fig. 25 is adopted to obtain the PSP at 120 Hz.

As shown in Fig. 25, the gain is 1 at 120 Hz, whereas the gains are 0 at 190, 260, and 330 Hz, meaning only the PSP at 120 Hz can remain through the CDSC.

Subsequently, by changing the frequency of unity gain to the other three frequencies, the four PSPs can be separated. In the condition without any external noise, the waveform in Fig. 26 can be obtained.

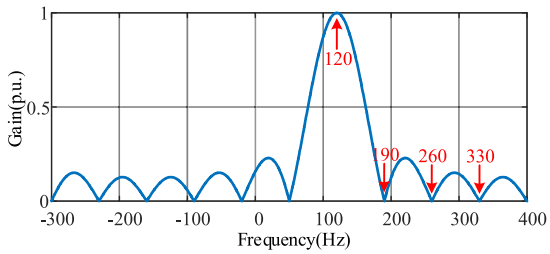

Fig. 25. Amplitude–frequency characteristic of the PSP separation CDSC.

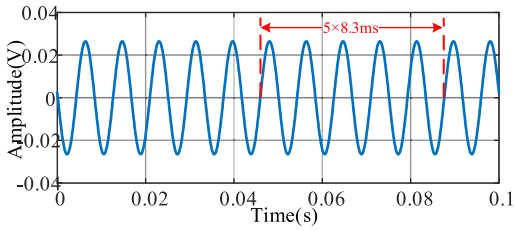

Fig. 26. Waveform of 120-Hz PSP extracted by the CDSC method without noise interference.

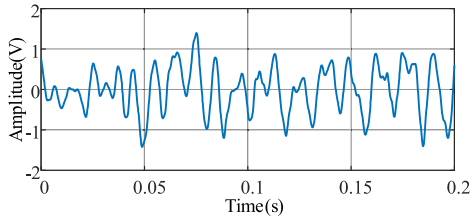

Fig. 27. Waveform of 120-Hz PSP extracted by the CDSC method with noise interference.

As shown in Fig. 26, from the period of the signal (8.3 ms), the frequency of the signal can be determined as 120 Hz. The current PSP can also be extracted by the same process. Note that the amplitude of the PSP is much smaller, which is due to the nonunity gain of the NSP-filter CDSC at 120 Hz, whereas, since the gain of the CDSC for the current and voltage signals are the same, the nonunity gain will not influence the accuracy of impedance calculation [24].

The CDSC method can retain the desired perturbation by eliminating the other components. The principle is excellent, and the influence of noise interference is not considered. For example, in the following, the random noise with the average values of 0.25 V and 0.4 A is generated by the noise generator and superimposed on the sampling signal. Then, the CDSC method is repeated, and the waveform of the extracted 120-Hz PSP is given in Fig. 27.

As shown in Fig. 27, the waveform is heavily distorted, according to which it is unable to extract the 120-Hz PSP. Such a result can be explained by the magnitude gain of the sum of the NSP filter process and the PSP separation process for the 120-Hz PSP, which is shown in Fig. 28.

According to Fig. 28, at 120 Hz, the gain is only 0.003, meaning that the perturbation is seriously weakened. Moreover, in most frequency bands, the magnitude gain is greater than that of 120 Hz. When there is noise interference, the noise at the other frequencies will remain and superimpose with each other.

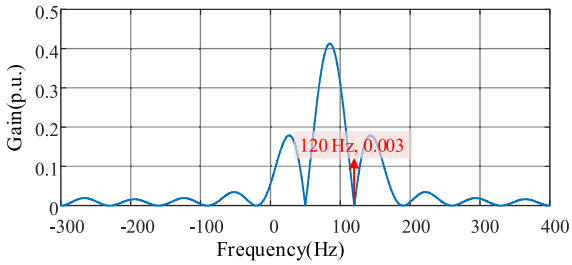

Fig. 28. Magnitude gain of the sum of the NSP filter process and the PSP separation process.

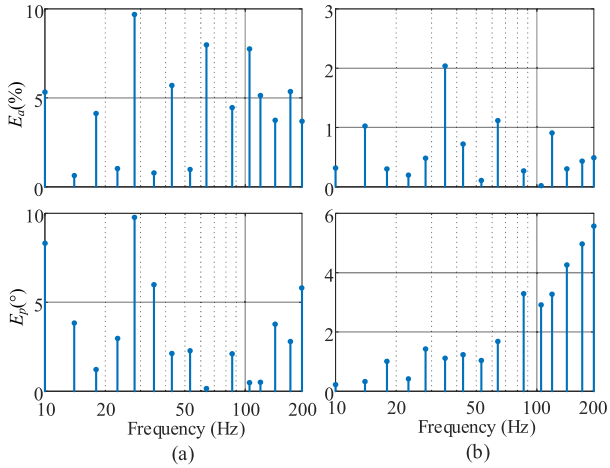

Fig. 29. Extraction errors for (a) $\boldsymbol{I}_{p2}[f_p - 2f_1]$ and (b) $\boldsymbol{V}_p[f_p]$ with noise interference.

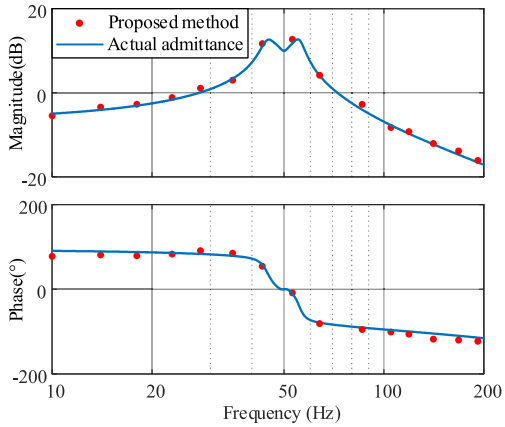

Fig. 30. Measurement results of Y_{21} with noise interference.

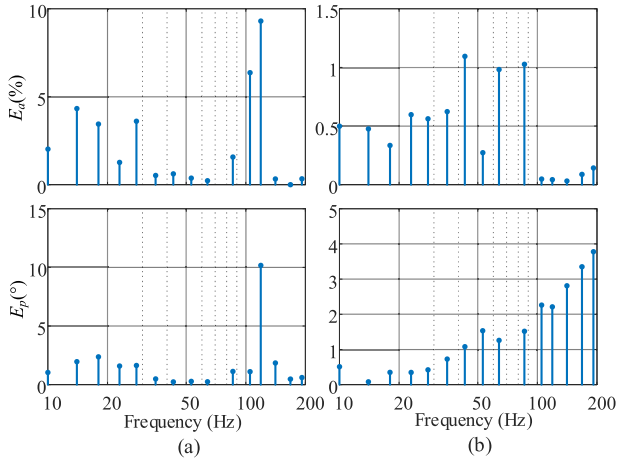

Fig. 31. Extraction error for (a) $\boldsymbol{I}_{p2}[f_p - 2f_1]$ and (b) $\boldsymbol{V}_p[f_p]$ when $f_1 = 50.3$ Hz.

Consequently, the waveform shown in Fig. 27 will be extracted. Therefore, since enough gain is not given to the PSP and the magnitude gain is not weak enough at the other frequencies, the noise-suppression ability of the CDSC method is required to be improved.

Another restriction of the CDSC method is that only a few frequencies with the same frequency interval can be measured at one time. It is known that due to the different complexity of the impedance characteristic in different frequency bands, frequencies with variable intervals are more effective than equal frequency intervals [11]. On the contrary, an equal frequency interval is not required while using the proposed method, which has higher flexibility in impedance measurement.

For comparison, under the same noise condition, the proposed method is also implemented. And the extraction errors of $\boldsymbol{I}_{p2}[f_p - 2f_1]$ and $\boldsymbol{V}_p[f_p]$ are given in Fig. 29.

From the figure, due to the noise interference, the extraction error is a little bigger than that without noise interference (see Fig. 22). However, the extracted signal still can obtain accurate measurement results, which are shown in Fig. 30. In the figure, the maximum magnitude error is only 1.36 dB, whereas the maximum phase error is only 14°, indicating the accuracy of the measurement results.

Since the proposed method adopts the amplitudes and phases of the two nearest and largest spectral lines, which is not seriously weakened compared with the original perturbation signal, as long as the injected perturbation signal has a sufficient SNR, the accuracy of the proposed method can be guaranteed.

When the fundamental frequency is 50.3 Hz, the proposed HW-DFT-based method is implemented. The extraction error of the proposed method is given in Fig. 31. According to the figure, the errors are lower than 10% and 11° for $\boldsymbol{I}_{p2}[f_p - 2f_1]$ and the errors are lower than 1.2% and 4° for $\boldsymbol{V}_p[f_p]$, revealing the effectiveness of the proposed method at different frequency deviations.

Based on the above-mentioned cases, when FFD occurs, the proposed method can accurately extract and subtract the deviated fundamental frequency, extract the coupling frequency signals, and help to obtain accurate measurement results. Moreover, compared with the existing method, the proposed method allows a much smaller frequency interval and has the better noise-suppression ability, which is beneficial to obtaining a more accurate impedance characteristic.

V. Conclusion

This article indicates the difficulty of measuring the frequency-coupling characteristic during FFD. The signal extraction method based on HW-DFT, which can precisely extract

measurement signals during SL, is proposed. The specific contribution of this article can be concluded as follows.

1) The deviation of the fundamental frequency may lead to inaccurate impedance measurement results, especially when the frequency-coupling characteristic exists. The reason for poor measurement accuracy is the insufficient frequency resolution and the occurrence of SL.
2) Based on the analysis of this article, when SL occurs, the distance between the real frequency and kf_r ($k = 0$, 1, 2, …) and the frequency-domain characteristic of the window function can determine the amplitude/phase–frequency characteristic of the fake spectra caused by SL. Accordingly, an HW-DFT-based method is proposed to accurately extract the measurement signals at coupling frequencies when SL occurs.
3) The effectiveness of the proposed method is verified by experimental cases based on the Typhoon CHIL platform. Compared with the existing method, the better flexibility and noise-suppression ability of the proposed method is also validated.

REFERENCES

[1] M. Cespedes and J. Sun, "Mitigation of inverter-grid harmonic resonance by narrowband damping," *IEEE J. Emerg. Sel. Topics Power Electron.*, vol. 2, no. 4, pp. 1024–1031, Dec. 2014.

[2] X. Wang and F. Blaabjerg, "Harmonic stability in power electronic based power systems: Concept, modeling, and analysis," *IEEE Trans. Smart Grid*, vol. 10, no. 3, pp. 2858–2870, May 2019.

[3] B. Hu, H. Nian, M. Li, Y. Xu, Y. Liao, and J. Yang, "Impedance-based analysis and stability improvement of DFIG system within PLL bandwidth," *IEEE Trans. Ind. Electron.*, vol. 69, no. 6, pp. 5803–5814, Jun. 2022.

[4] H. Nian, J. Yang, B. Hu, Y. Jiao, Y. Xu, and M. Li, "Stability analysis and impedance reshaping method for DC resonance in vscs-based power system," *IEEE Trans. Energy Convers.*, vol. 36, no. 4, pp. 3344–3354, Dec. 2021.

[5] B. Wen, D. Boroyevich, R. Burogos, P. Mattavelli, and Z. Shen, "Analysis of D-Q small-signal impedance of grid-tied inverters," *IEEE Trans. Power Electron.*, vol. 31, no. 1, pp. 675–687, Jan. 2016.

[6] M. Cespedes and J. Sun, "Impedance modeling and analysis of grid-connected voltage-source converters," *IEEE Trans. Power Electron.*, vol. 29, no. 3, pp. 1254–1261, Mar. 2014.

[7] I. Vieto and J. Sun, "Sequence impedance modeling and analysis of type-III wind turbines," *IEEE Trans. Energy Convers.*, vol. 33, no. 2, pp. 537–545, Jun. 2018.

[8] Y. Xu, H. Nian, T. Wang, L. Chen, and T. Zheng, "Frequency coupling characteristic modeling and stability analysis of doubly fed induction generator," *IEEE Trans. Energy Convers.*, vol. 33, no. 3, pp. 1475–1486, Sep. 2018.

[9] B. Hu, H. Nian, M. Li, Y. Liao, J. Yang, and H. Tong, "Impedance characteristic analysis and stability improvement method for DFIG system within PLL bandwidth based on different reference frames," *IEEE Trans. Ind. Electron.*, vol. 70, no. 1, pp. 532–543, Jan. 2023.

[10] H. Nian, M. Li, B. Hu, L. Chen, and Y. Xu, "Design method of multisine signal for broadband impedance measurement," *IEEE J. Emerg. Sel. Topics Power Electron.*, vol. 10, no. 3, pp. 2737–2747, Jun. 2022.

[11] M. Li, H. Nian, B. Hu, Y. Xu, Y. Liao, and J. Yang, "Adaptive frequency adjustment method for impedance measurement," *IEEE J. Emerg. Sel. Topics Power Electron.*, vol. 10, no. 1, pp. 518–531, Feb. 2022.

[12] T. Roinila, M. Vilkko, and J. Sun, "Broadband methods for online grid impedance measurement," in *Proc. IEEE Energy Conver. Congr. Expo.*, 2013, pp. 3003–3010.

[13] T. Roinila, M. Vilkko, and J. Sun, "Online grid impedance measurement using discrete-interval binary sequence injection," *IEEE J. Emerg. Sel. Topics Power Electron.*, vol. 2, no. 4, pp. 985–993, Dec. 2014.

[14] J. Sihvo, D.-I. Stroe, T. Messo, and T. Roinila, "Fast approach for battery impedance identification using pseudo-random sequence signals," *IEEE Trans. Power Electron.*, vol. 35, no. 3, pp. 2548–2557, Mar. 2020.

[15] Z. Yang, W. Liao, Q. Zhang, C. L. Bak, and Z. Chen, "Fault coordination control for converter-interfaced sources compatible with distance protection during asymmetrical faults," *IEEE Trans. Ind. Electron.*, to be published, doi: 10.1109/TIE.2022.3204946.

[16] J. Sihvo, T. Messo, T. Roinila, and R. Luhtala, "Online internal impedance measurements of Li-ion battery using PRBS broadband excitation and fourier techniques: Methods and injection design," in *Proc. IEEE Int. Power Electron. Conf.*, 2018, pp. 2470–2475.

[17] J. Sihvo, T. Messo, T. Roinila, R. Luhtala, and D. I. Stroe, "Online identification of internal impedance of Li-ion battery cell using ternary-sequence injection," in *Proc. IEEE Energy Convers. Congr. Expo.*, 2018, pp. 2705–2711.

[18] T. Roinila, H. Abdollahi, S. Arrua, and E. Santi, "Real-time stability analysis and control of multiconverter systems by using MIMO-identification techniques," *IEEE Trans. Power Electron.*, vol. 34, no. 4, pp. 3948–3957, Apr. 2019.

[19] H. Hu, P. Pan, Y. Song, and Z. He, "A novel controlled frequency band impedance measurement approach for single-phase railway traction power system," *IEEE Trans. Ind. Electron.*, vol. 67, no. 1, pp. 244–253, Jan. 2020.

[20] X. Weng, Z. Zhao, K. Chen, and L. Yuan, "Chirp signal injection method and real-time impedance characteristic measurement of electric energy router," *IEEE J. Emerg. Sel. Topics Power Electron.*, vol. 10, no. 5, pp. 5564–5577, Oct. 2022.

[21] H. Gong, X. Wang, and D. Yang, "DQ-frame impedance measurement of three-phase converters using time-domain MIMO parametric identification," *IEEE Trans. Power Electron.*, vol. 36, no. 2, pp. 2131–2142, Feb. 2021.

[22] M. Li, H. Nian, B. Hu, Y. Xu, Y. Liao, and J. Yang, "Design method of multi-sine signal for broadband impedance measurement considering frequency coupling characteristic," *IEEE J. Emerg. Sel. Topics Power Electron.*, vol. 10, no. 1, pp. 532–543, Feb. 2022.

[23] P. Zhong, J. Sun, Z. Tian, M. Huang, P. Yu, and X. Zha, "An improved impedance measurement method for grid-connected inverter systems considering the background harmonics and frequency deviation," *IEEE J. Emerg. Sel. Topics Power Electron.*, vol. 9, no. 4, pp. 4236–4247, Aug. 2021.

[24] P. Zhong, J. Sun, Z. Tian, P. Yu, and X. Zha, "CDSC-based adaptive impedance measurement method for grid-tied inverter system under adverse grid voltage conditions," *IEEE Trans. Ind. Electron.*, vol. 69, no. 11, pp. 11210–11220, Nov. 2022.

[25] K. F. Chen and S. L. Mei, "Composite interpolated fast fourier transform with the Hanning window," *IEEE Trans. Instrum. Meas.*, vol. 59, no. 6, pp. 1571–1579, Jun. 2010.

[26] J. Castello and J. M. Espi, "DSP implementation for measuring the loop gain frequency response of digitally controlled power converters," *IEEE Trans. Power Electron.*, vol. 27, no. 9, pp. 4113–4121, Sep. 2012.

[27] F. W. Isen, *DSP for MATLAB™ and LabVIEW™ II: Discrete Frequency Transforms*. Berlin, Germany: Springer, 2009.

[28] J. G. Proakis, *Algorithms For Statistical Signal Processing*. Beijing, China: Tsinghua Univ. Press, 2003.

[29] A. V. Oppenheim, A. S. Willsky, and S. Hamid, *Signals and Systems*. Englewood Cliffs, NJ, USA, Prentice-Hall, 1996.

[30] H. Zappen, F. Ringbeck, and D. U. Sauer, "Application of time-resolved multi-sine impedance spectroscopy for lithium-ion battery characterization," *Batteries*, vol. 4, no. 4, Dec. 2018, Art. no. 64.

Meng Li (Graduate Student Member, IEEE) was born in Chifeng, China. He received the B.Eng. degree in electrical engineering in 2019 from Zhejiang University, Hangzhou, China, where he is currently working toward the Ph.D. degree in electrical engineering.

His research interests include small-signal stability analysis of grid-connected operations and the technology for impedance measurement of renewable generators.

Heng Nian (Senior Member, IEEE) received the B.Eng. and M.Eng. degrees in electrical engineering from the Hefei University of Technology, Hefei, China, in 1999 and 2002, respectively, and the Ph.D. degree in electrical engineering from Zhejiang University, Hangzhou, China, in 2005.

From 2005 to 2007, he was a Postdoctoral Researcher with the College of Electrical Engineering, Zhejiang University, where he became an Associate Professor in 2007 and has been a Full Professor of electrical engineering since 2016. From 2013 to 2014, he was a Visiting Scholar with the Department of Electrical, Computer, and System Engineering, Rensselaer Polytechnic Institute, Troy, NY, USA. His current research interests include optimal design and operation control for wind power generation systems. He has published more than 40 IEEE/IET Transaction papers and holds more than 20 issued/pending patents.

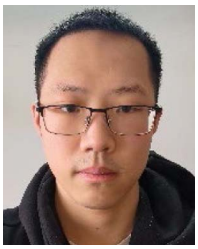

Han Li was born in Changde, China. He received the B.Eng. degree in electrical engineering in 2021 from Zhejiang University, Hangzhou, China, where he is currently working toward the Ph.D. degree in electrical engineering.

His research interests include the impedance measurement of renewable generators.

Bin Hu (Student Member, IEEE) was born in Wenzhou, China. He received the B.Eng. degree in electrical engineering from the Shenyang University of Technology, Shenyang, China, in 2018. He is currently working toward the Ph.D. degree in electrical engineering at Zhejiang University, Hangzhou, China.

From 2021 to 2022, he was a Visiting Student with the Department of Energy Technology, Aalborg University, Aalborg, Denmark. His research interests include large-signal and small-signal synchronization stability of converter-based resources, especially doubly fed induction-generator-based wind power systems.

Mr. Hu was a recipient of the Best Paper Award of IEEE TRANSACTIONS ON ENERGY CONVERSION in 2022.

Yuming Liao (Graduate Student Member, IEEE) was born in Ganzhou, Jiangxi, China. He received the M.Eng. degree in electronics and power transmission from the Department of Electrical Engineering, Hefei University of Technology, Hefei, China, in 2018. He is currently working toward the Ph.D. degree in electrical engineering at Zhejiang University, Hangzhou, China.

His research interests include stability analysis of grid-connected operations and wind power generation systems.

Haipan Li was born in Linfen, China. He received the B.Eng. degree in electrical engineering from Zhejiang University, Hangzhou, China, in 2020. He is currently working toward the Ph.D. degree in electrical engineering with Zhejiang University, Hangzhou, China.

His research interests include small-signal modeling of renewable generators, their integration to the electric grid and system stability analysis.

Yiming Liu was born in Jining, China. He received the B.Eng. degree in electrical engineering from the Hefei University of Technology, Hefei, China, in 2020. He is currently working toward the M.Eng. degree in electrical engineering at Zhejiang University, Hangzhou, China.

His research interests include small-signal modeling of LCC high-voltage direct current, its impedance characteristic analysis, and system stability analysis.

Yaoxin Wang was born in Changzhi, China. He received the B.Eng. degree in electrical engineering in 2021 from Zhejiang University, Hangzhou, China, where he is currently working toward the M.Eng. degree in electrical engineering.

His research interests include the dc-impedance-based stability analysis methods for voltage-source-converter-based power systems under weak grids and the corresponding impedance reshaping control strategy.